

## **Chapter 22**

### **Optimization of X-ray Radiographic Imaging**

**Birsen Yazici, Il-Young Son, An Jin**

#### **Synopsis**

This chapter presents x-ray image quality optimization techniques using digital phantom images and computerized observer models. The X-ray imaging parameters are optimized so as to maximize tumor detectability while minimizing the patient dose. Digital phantoms are generated using the virtual photographic and radiographic imaging simulator (ViPRIS) package. ViPRIS uses a tomographic phantom, VIP-Man, constructed from Visible Human anatomical color images to simulate the scattered portion using the ESGnrc Monte Carlo code. The primary portion of an x-ray image is simulated using the projection ray-tracing method through the Visible Human CT data set. To produce a realistic image, the software simulates quantum noise, blurring effects, lesions, detector absorption efficiency and other imaging artefacts. The primary and scattered portions of an x-ray chest image are combined to form a final image for computerized observer studies and image quality analysis. Absorbed doses in organs and tissues of the segmented VIP-Man phantom are obtained from the Monte Carlo simulations. Tumor detectability is determined by Receiver Operating Characteristic (ROC) methodology. Hotelling and Laguerre–Gauss Hotelling observers are used to perform various lesion detection tasks. Several model observer tasks were used including SKE/BKE, MAFC and SKEV. The energy levels and fluence at the minimum dose required to detect a small lesion were determined with respect to lesion size, location and system parameters. The purpose of combining computerized observers and digital phantoms is to develop quantitative image quality metrics and simulate human subjects

in order to analyze a volume of data that would otherwise be impossible to handle with actual human subjects.

## **1. Introduction**

In the United States, approximately 250 million radiological examinations are performed each year, making diagnostic medical examinations the largest source of man-made radiation exposure (UN 2000). A major goal of radiography is to maximize the amount of diagnostic information while minimizing the radiation exposure to the patient. All radiographic x-ray examinations require the selection of beam parameters, which affect both the patient dose and the corresponding image quality. Optimization is difficult because of the following reasons:

- (i) The x-ray imaging chain contains a large number of variables associated with the x-ray beam characteristics, patient anatomy, scatter removal grid, and x-ray detector system.
- (ii) Diagnostic x-ray examinations involve various body sites and tasks.
- (iii) Effective dose is the sole indicator of patient risk but is not obtainable without a whole-body phantom of delineated organs.
- (iv) The images must be evaluated by an observer with respect to a quantitative image quality criteria and determine if the images meet the criteria.

To model the generation of a radiograph, we have developed the Virtual Photographic and Radiographic Imaging Simulator (ViPRIS) (Winslow, Xu & Yazici 2005). At the core of this simulator are the image sets that have been made available to the public by the United States National Library of Medicine's Visible Human Project (VHP) (Spitzer & Whitlock 1998). The user is permitted to specify different grid filtering parameters, detector efficiency, and nodules of varying composition and their location. A simple user-friendly software interface permits a user to develop thousands of simulated images and data sets to investigate the

relationship between lesion detection threshold, lesion characteristics, patient dose, detector efficiency, and x-ray beam characteristics.

Previous related work in computer simulations of x-ray imaging chain include (Lazos, Bliznakova, Kolitsi & Pallikarakis 2003) and (Sandborg, McVery, Dance & Carlsson 2001). In (Lazos et al. 2003), a simulated x-ray system was developed which included several modules such as; Monte Carlo modeling of the particle beam with variable spectrums (kVp), grid transmission rates, image formation, and voxel dose calculation. The phantom was built from a composite of geometric primitives. Our objective differs from Lazos' group in that we seek to optimize the imaging chain by providing satisfactory image quality while at the same time minimizing the patient's dose. Also, our phantom is derived from VHP images, providing a more accurate model. Sandborg's group used CT images for head-torso, with coarser resolutions than those from VHP, to build their phantom. Our approach also deviates from Sandborg's in that their image quality measure is based on explicit calculation of optical density differences (using Monte Carlo simulations). In contrast, to evaluate the image quality, we have used computerized observers in series of simulated experiments.

The motivation for studying image quality using simulated observers rests on the fact that conducting human observer studies requires a large amount of time and effort. Optimizing the imaging process requires repeating observer studies many times with a large number of images until the ideal settings can be determined. As an example of the scale of data needed for reliable results, our own study utilized approximately 2,500,000 images. Such a large scale survey is untenable using human subjects. Computerized observer studies have, in recent year, been applied to X-ray image quality analysis. These techniques assess quality by how well a simulated observer detects the presence (or absence) of a lesion. Several different type of simulated observers have

been developed including Hotelling, channelized Hotelling, and non-prewhitening matched filter with eye filter (NPWE) (Pineda & Barret 2004a, Pineda & Barret 2004b, Eckstein, Abbey & Bochud 2000). The purpose is to develop quantitative image quality metrics and simulate human subjects in order to analyze volume of data that would otherwise be impossible to handle with actual human subjects. Our study examines the utility of such a method in conjunction with ViPRIS for optimizing x-ray imaging. Optimization is performed with respect to two opposing objectives, 1) to maximize the detectability of a lesion and 2) to minimize the dosage administered to the patient. Toward this goal, we have developed an image analysis system with computerized observers using Matlab. We have implemented two observer models, the Hotelling, Laguerre-Gauss Hotelling. We have used SKE/BKE, MAFC, and SKEV observer tasks for analysis (Abbey, Barrett & Eckstein 1997). We have used the AUC and probability of correct detection as our image quality metrics.

Optimization of the radiography process occurs using three distinct modules.

ViPRIS is used to produce realistic chest x-ray images and represents the first module.

The second module is the VIP-Man phantom and the dosimetry calculations within

EGSnrc (Kawrakow & Rogers 2003). Our Matlab code analyzes the quality of the

images and represents the third module. The effective dose of each image representing

a specific quality are plotted to find the minimum effective dose for the configuration

specified by the user.

## **2. Digital phantom generation and effective dose calculations**

### ***2.1. Background of ViPRIS***

ViPRIS represents a first generation imaging simulator that strives to produce realistic images

using a simulation that authentically reproduces the process of obtaining a radiograph (Winslow et

al. 2005). At the core of VIPRIS are the image sets that have been made available to the public by the United States National Library of Medicine's Visible Human Project (VHP). ViPRIS utilizes two phantoms constructed from identical anatomy of the VHP. The simulated production of images is split into two steps. An image projection phantom constructed from the CT data set is used to simulate primary x-rays using a ray-tracing technique. Scattered x-rays are simulated using the Visible Photographic Man tomographic phantom (VIP-Man) previously constructed from segmented color cryosectional photographs of the VHP (Xu, Chao & Bozkurt 2000). The VIP-Man phantom was originally developed from the VHP cryosectional photographs to calculate radiation doses to an adult male. Image data from the VHP includes four sets of images. CT, MRI and X-ray images were obtained of the fresh body. The body was then frozen to allow 1-mm thick slices to be removed from head to toe for cross-sectional color photographs. At the end of the VHP, a total of 1878 transverse color photographs were obtained and segmented to identify approximately 1400 organs and tissues of interest for the male cadaver to form a digital atlas of what was called the "Visible Man." At Rensselaer Polytechnic Institute, segmentation and classification were performed to finally adopt 72 radiosensitive organs and tissues for radiation dosimetry studies in EGSnrc. Values of tissue densities and compositions for radiation dosimetry calculations were based on those recommended in ICRP 23 (ICPR 1975). The original voxel size of the VIP-Man model is 0.33 mm x 0.33 mm x 1 mm. The whole body is represented by 3,384,606,720 voxels. To reduce the computational burden a simplified version of VIP-Man with a resolution of 1 mm x 1 mm x 1 mm was used for this study. The EGSnrc code is used in our program to calculate organ doses as well as to develop the scatter images. Because patients are instructed to lift their arms out of the field, for this study modifications were made to the VIP-Man phantom to remove the arms.

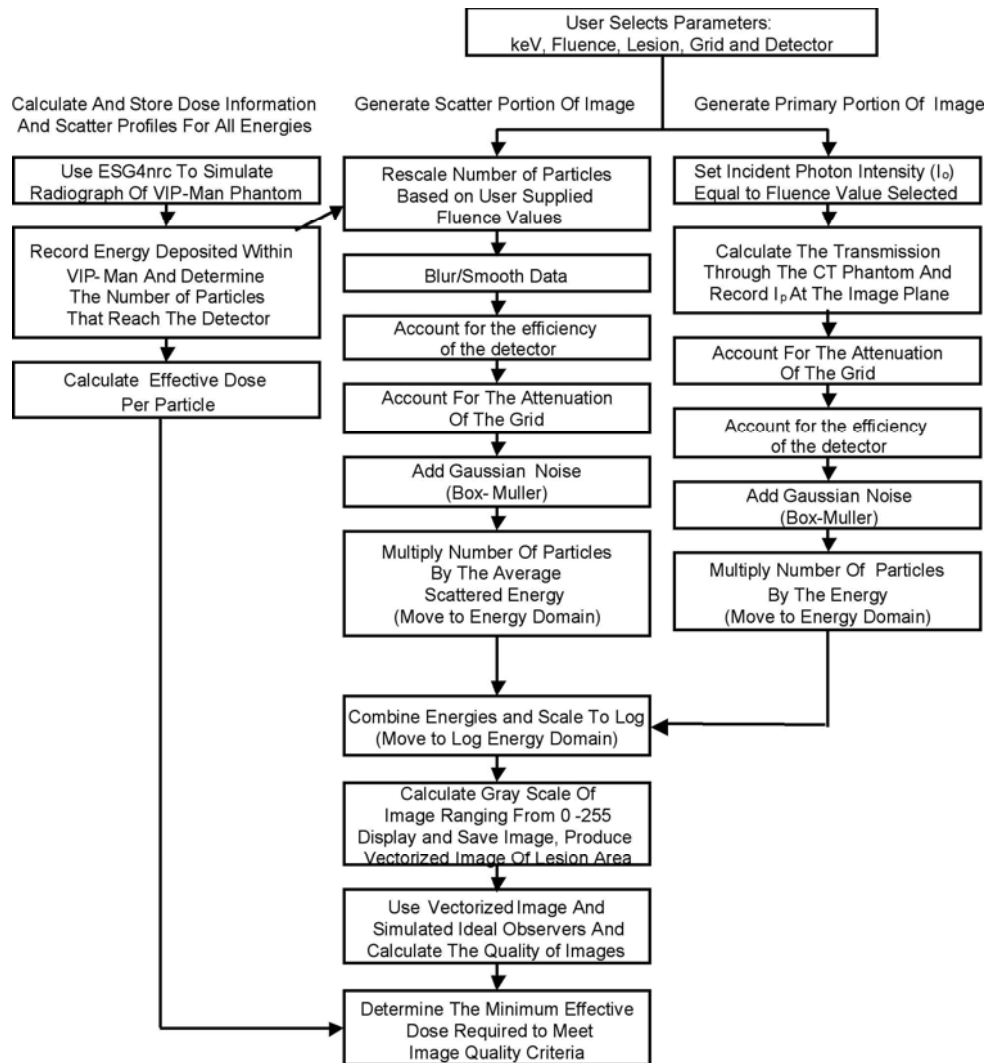


Figure 1. Flow chart of x-ray simulation and optimization process using ViPRIS and image quality analysis.

## 2.2. The process of image generation

Generation of simulated images is done in two phases. For a given x-ray characteristics (such as the number of photons and energy), ViPRIS calculates the primary x-ray intensity (i.e., transmitted x-rays) by tracing each x-ray through the Image Projection Phantom. ViPRIS then scales and calculates the scattered x-rays based on stored data files from pre-generated Monte Carlo simulations. The scattered data set is smoothed to remove excess noise caused by statistical variations inherent in Monte Carlo simulations. Each data set is modified based on the specified

detector quantum efficiency. Quantum noise is added to the primary and scattered images using Box-Muller approximation of a Gaussian distribution as described in (Box & Muller 1958, Winslow 2005). Finally, the two images are combined to form the simulated radiograph. The flow of the process is illustrated in Figure 1. The details of each step of the process are given below.

The primary portion of an x-ray image is formed by photons that transmit through patient anatomy without interactions. Visible Human CT data can be converted into tissue specific attenuation coefficients. Using the tissue specific attenuation coefficient data and Beer-Lamberts law the number of transmitted photons is calculated for each pixel using the fluence (i.e. the number of photons per unit area) specified by the user. To simulate lesions, ViPRIS replaces attenuation coefficients of certain voxels within the selected chest region of the CT with those of lesions. The software allows a user to select a variety of lesion geometries and compositions in the form of a lesion Hounsfield Units (HU) (Winslow et al. 2005).

When an x-ray photon enters the patient body, there is a probability that an x-ray may undergo scattering off the intended path and towards the film or detector grid resulting in an added random background noise to the primary image. Monte Carlo techniques are ideally suited for modeling this random process. Because the probability of Compton scattering is relatively small for x-rays and a large number of particle histories are necessary to reduce the statistical uncertainty inherent in the Monte Carlo method this process was extremely time consuming and required approximately 2 days for simulation over 40 keV and 10 days for 30 and 35 keV. Therefore, we chose to simulate each energy once and store the resulting image. A sample image can be seen in Figure 2. To further reduce the statistical uncertainty (mottle or noise), each data set is soothed or denoised using a 24 x 24 boxcar filter (Box & Muller 1958). Once the primary and scatter images are calculated, ViPRIS accounts for various imaging components detailed below and forms



**Figure 2. A sample output of ViPRIS showing a simulated chest x-ray image.**

a final image. Prior to any operations the scatter data is scaled to match the fluence specified by the user. ViPRIS uses an approximation of a Gaussian distribution to add simulated quantum noise to the primary and scatter image data. The square root of the number of photons incident on a pixel is used to simulate the standard deviation of noise as governed by Gaussian statistics. Because the quantum absorption efficiency (detection efficiency) of the detector is not unity, the user specified efficiency for the primary and average scattered energies are used to modify the number of particles detected in all scattered and primary pixels. This allows for the simulation of any detector as well as x-ray system.

To convert the photon fluence of the primary image into energy fluence, the number of surviving particles in each pixel is multiplied by the user specified energy. For the scattered portion the same procedure is followed; however, the average scatter particle energy is used. To

combine the scatter and primary portions of the radiograph, the specifications of the user-defined grid are utilized. ViPRIS simulates the presence of a grid by allowing the user to specify the transmission percentages of the primary and scattered image. The data set is then scanned for the lowest and highest numbers. The lowest log energy fluence is then subtracted from each data point. A new maximum is calculated and divided by 255. The data is then converted into a gray scale value between 0 and 255.

### ***2.3. Calculation of effective dose***

Organs receive x-ray doses from secondary electrons resulting from photoelectron absorption and Compton scattering. During the formation of the scatter profile the energy deposition in each of the major organs of the VIP-Man model is saved. The mean absorbed dose in an organ or tissue ( $D_T$ ) is calculated as the total energy deposited in organ  $T$  divided by the organ mass. The equivalent dose ( $H_T$ ) in organ  $T$  is calculated by multiplying the mean absorbed dose by the radiation-weighting factor,  $w_R$ , which is unity for photons and electrons. Since the same equivalent dose value can cause different risk in different organs or tissues, a tissue weighting factor ( $w_T$ ), has to be applied to yield the total risk, in terms of effective dose ( $E$ ) using Equation (1) (ICPR 1991).

$$E = \sum w_T H_T \quad (1)$$

A thin layer of fat tissue around chest level is used as male breast. Ten more organs and tissues are included in the remainder group of organs which together shares a total tissue weighting factor of 0.05.

Monoenergetic photons were considered in ViPRIS for dose calculations. The user specifies the energy to be used for each simulation. For each pre-generated scattered image there is a corresponding dosimetry data set. When the scatter data file is loaded the associated dosimetry

data set is also specified. The data set contains conversion factors for effective dose per particle at the specified energy. Since the user specifies a fluence to be simulated an effective dose is calculated by multiplying the dose conversion factor by the fluence (Winslow, Huda, Xu, Chao, Shi, Ogden & Scalzetti 2004).

### **3. Image Quality Analysis**

In recent years, there has been extensive work on simulating the response of observers using computer models. The field has increasingly become a standard means of evaluating quality of medical images in research. A non-prewhitening matched filter was used to study wavelet-based compression (Zhao, Schwarz & Kijewski 1998). Performance of JPEG2000 compression was studied using non-prewhitening matched filter with eye filter, Hotelling and channelized Hotelling (Eckstein, Bartroff, Abbey, Whiting & Bochud 2003, Suryanarayanan, Karellas, Vedantham, Ved & D'Orsi 2003). Image quality metrics for model observers in digital radiography was studied for uniform and structured backgrounds (Pineda & Barret 2004a, Pineda & Barret 2004b). More recently, observer study was conducted for tomographic image reconstruction (Yendiki & Fessler 2005). In this work, we use image quality analysis as a tool for selecting optimal fluence and energy levels for the purposes of detecting lesions while keeping the patient dose at a minimum.

#### **3.1. Observer models**

The observer's task is to take an image and decide whether the image contains a lesion or not. In general, such tasks are known as signal detection task. Each observer makes its decision based on a test statistic,  $\lambda$ , calculated using the input image and statistics derived from a given set of training data. In the case of linear observer models, the equation for  $\lambda$  is simply

$$\lambda = w^T g \quad (2)$$

where  $w$  is the template used by the observer and  $g$  is the vectorized test image. The decision is

made by comparing  $\lambda$  to a threshold, i.e. if  $\lambda$  is below the threshold the image is classified as background, else it is classified as containing a lesion. Two main model observers are used in this study.

*a) Hotelling observer* Under the Gaussian noise assumption, Hotelling observer is an optimal linear observer, maximizing the signal-to-noise ratio (SNR) of the test statistic. It can be derived from the Bayesian decision rule given that the noise is additive and Gaussian. The Hotelling observer uses first and second order statistics (for both lesion and no-lesion images) to calculate its template. The template for Hotelling observer is given by (Pineda & Barret 2004a)

$$w_h = \Sigma^{-1}(\bar{g}_l - \bar{g}_b) \quad (3)$$

where  $(\bar{g}_l, \Sigma_l)$  and  $(\bar{g}_b, \Sigma_b)$  denote the sample mean and covariance matrices of the lesion and background images, respectively; and  $\Sigma = (\Sigma_l + \Sigma_b)/2$  is the average of the two covariance matrices. Since  $\Sigma$  is symmetric, so is  $\Sigma^{-1}$ . Therefore, Equation (2) becomes

$$\lambda = (\bar{g}_l - \bar{g}_b)\Sigma^{-1}g \quad (4)$$

*b) Channelized and Laguerre-Gauss Hotelling observers* A modification to the Hotelling observer was previously shown in (Yao & Barrett 1992) to yield a good fit to a human observer. This modified observer is generally known as channelized Hotelling observer. In this study, Laguerre-Gauss channelized Hotelling observer is used as described in (Barrett, Abbey, Gallas & Eckstein 1998). In a generic channelized Hotelling observer, the images are first filtered through a set of frequency selective ‘‘channels’’ (Myers & Barrett 1987). The template is calculated based on the filtered training images, then it is applied to the filtered test images. Let  $U$  represent a matrix with each column equal to a channel, then the covariance matrix of the channelized images are

$$\Sigma_{ch} = U^T \Sigma U \quad (5)$$

and the template is equal to

$$w_{ch} = \Sigma_{ch}^{-1} U^T (\bar{g}_s - \bar{g}_b) \quad (6)$$

Using Equation (6), one can derive the test statistic  $\lambda$  of the channelized Hotelling observer as follows:

$$\lambda = (\bar{g}_s - \bar{g}_b)^T U \Sigma_{ch}^{-1} U^T g \quad (7)$$

In this study, each filter is a Laguerre-Gauss function of different order. A Laguerre-Gauss function is nothing but the product of Gaussian function with the n-th order Laguerre polynomial,

$$U_n(r, a) = \frac{2\sqrt{\pi}}{a} \exp\left(\frac{-\pi r^2}{a^2}\right) L_n\left(\frac{2\pi r^2}{a^2}\right) \quad (8)$$

where  $L_n(x)$  is the n-th order Laguerre polynomial given by

$$L_n(x) = \sum_{m=0}^n (-1)^m \binom{n}{m} \frac{x^m}{m!} \quad (9)$$

A total of five channels were used in this study, using zero to fourth order Laguerre polynomials.

### 3.2. Task Descriptions

(a) *SKE/BKE*      The simplest image quality analysis is the signal known exactly /background known exactly or SKE/BKE task (Abbey et al. 1997). In such a case, each image location is fixed, i.e. the background remains fixed and the form of the "signal", i.e. lesion, being detected is known exactly prior to the analysis with no variations from trial to trial. The only variation comes from the random noise in the image due to quantum mottle. In this case, a single template is created for the computerized observers using statistics derived from lesion and background images as described previously. At each trial, the simulated observer is presented with an image taken at the same exact location. The observer's task is to determine whether or not

a lesion is present in the image. This is achieved by the computerized observer by setting a threshold value, say  $\lambda_0$ , and applying a simple decision function. The decision function,  $D$  is a function of  $\lambda_0$  and is given by

$$D(\lambda; \lambda_0) = u(\lambda - \lambda_0) \quad (10)$$

where  $u(x)$  is a unit step function which equals to 1 when  $x \geq 0$  and 0, otherwise.  $D(\lambda; \lambda_0) = 1$  indicates detection of a lesion. Due to the simplicity of the SKE/BKE task, it is not a good representative of real world clinical situations. The task lacks the variability in the background and lesion that is present in a real world situation.

(b) *MAFC* Two alternative forced choice (2AFC) and its generalization, M alternative forced choice (MAFC) tasks extends SKE/BKE by introducing variations in the lesion location (Abbey et al. 1997, Burgess & Ghandeharian 1984). In these tasks, an observer is presented with a set of M images each at different locations. The set of locations are fixed. Only one of these images contains the lesion. The form of the lesion (shape and size) being detected is known exactly and is fixed prior to analysis. The observer's goal is to determine the location that contains the lesion. As with SKE/BKE, a single template is generated for the task based on training samples with various backgrounds. The optimal solution to MAFC task can be derived given that each locations are pairwise uncorrelated. The task procedure is then to apply this template to each locations and select the one with the highest  $\lambda$  value to be the location with the lesion.

(c) *SKEV and SKS* The MAFC task, although more realistic than SKE/BKE, still assumes a static lesion morphology. To implement a more realistic task, the MAFC can be further generalized to incorporate variations in the form of the lesion itself. There are two kinds of such tasks, signal known exactly but varied (SKEV) and signal known statistically (SKS). Both approaches have been studied in (Eckstein & Abbey 2001) and (Eckstein, Bartroff, Abbey,

Whiting & Bochud 2003) and begin with a predetermined set of signals and backgrounds. Suppose  $J$  types of lesions, which may vary in any number of ways from shape or size to physiological characteristic of the lesion, are given and that  $M$  set of locations that may contain the lesion are identified. In SKEV task, the observer is presented with the  $M$  locations and knows a priori what lesion type to look for. The goal is to identify which of the  $M$  locations contains this form of the lesion. As with MAFC, only one location contains the lesion at each trial. With computerized observers, this procedure translates to identifying the location that gives the highest  $\lambda$  value when applying a template specific to the type of lesion. Thus, a separate template must be generated for each lesion type using the appropriate set of training data. Although SKEV task takes lesion variations into account it does so with a priori knowledge about the type of lesion present for each trial. Thus, under the assumption that the locations are pairwise uncorrelated, SKEV is no different than an MAFC task at each individual trial. The introduction of the lesion variation from trial to trial, however, does effect the performance of the observer. The SKS task does not use this a priori information. The task remains fundamentally the same; that is, choose the location that contains the lesion. However, now the observer's uncertainty about the lesion variation is also taken into account. As with SKEV task, a set of  $J$  templates are computed, one for each lesion type. However, unlike SKEV task, SKS is performed in two steps. First,  $J \times M$  set of test statistics are generated, one for each lesion type and each location. Then these templates are combined to produce a "sum-of-likelihood" value for a lesion being present in a given location, where the sum is over all lesion types. Assuming  $J$  number of lesion variations and  $M$  pairwise uncorrelated locations, this likelihood for the  $i$ -th location is given as

$$l_i = \sum_{j=1}^J \left[ \frac{1}{\sigma_j \sqrt{2\pi}} \right]^M \exp\left(-\frac{(\lambda_{i,j} - \bar{\lambda}_{1,j})^2}{2\sigma_j^2}\right) \prod_{m=1}^M \left[ \exp\left(-\frac{(\lambda_{m,j} - \bar{\lambda}_{0,j})^2}{2\sigma_j^2}\right) \right]^{(1-\delta_{m,j})} \quad (11)$$

where  $\delta_{m,j}$  denotes the Kronecker's delta,  $\bar{\lambda}_{1,j}(\bar{\lambda}_{0,j})$  is the statistical expectation of the test statistic if the j-th type lesion is present (not present),  $\lambda_{i,j}$  is the test statistic at the i-th location for the j-th type lesion. The location with the largest  $l_i$  is determined to be the location where the lesion is present.

### 3.3. Performance Measures

As a measure of quality for SKE/BKE and 2AFC images, receiver operator characteristic (ROC) curve and the area under the ROC curve (AUC) are calculated and plotted for each simulated observers. These curves are often used as measure of image quality and have been studied extensively in other fields such as target detection in radar. The idea is to examine the AUC for varying fluence and energy levels to estimate the optimal dose to achieve desired performance in lesion detection. The ROC is a plot of sensitivity versus one minus the specificity as a function of threshold level. Sensitivity is given as the ratio between the number of true positives and the total number of actually positive cases

$$sensitivity = \frac{N_{TP}}{N_{TP} + N_{FN}} \quad (12)$$

where NTP is the number of true positives and NFN is the number of false negatives. Specificity, on the other hand, is given by the ratio between the number of true negatives and the total number of negative results

$$specificity = \frac{N_{TN}}{N_{TN} + N_{FP}} \quad (13)$$

where NTN is the number of true negatives and NFP is the number of false negatives. Specificity, therefore, can be seen as a measure of how meaningful a positive decision is. By varying the threshold of detection, the level of specificity and sensitivity changes. At a low detection threshold,

we expect a low level of specificity and high level of sensitivity and vice versa. A good measure of image quality is the AUC. A linear ROC curve with AUC of 0.5 indicates an observer whose decision is essentially random and suggests that image quality is poor; whereas a steep rise in ROC curve, corresponding to AUC close to 1, indicates high image quality, providing high sensitivity and specificity. The characteristics of the AUC suggests a probabilistic interpretation. In fact, if one interprets the test statistic score as a ranking criteria, it can be shown that AUC is equivalent to the probability of test statistic score for lesion ranking higher than the test statistic score for the background (Agarwal, Graepel, Herbrich, Har-Peled & Roth 2005). The ROC and thus the AUC curves apply only to simple binary classification tasks and cannot be constructed for MAFC, SKEV, and SKS, where the task detection and location of a lesion vary leaving more than two alternatives for an answer. Taking cue from the probabilistic interpretation of the AUC, an alternative metric of image quality can be derived for MAFC, SKEV, and SKS tasks based on probability of lesion score ranking above background. For MAFC, under the assumption that the M locations are pairwise uncorrelated, P is estimated as

$$P = \frac{1}{N} \sum_{n=1}^N u(\lambda_{1,n} - \max(\lambda_{0,n})) \quad (14)$$

where N is the total number of trials,  $\lambda_{1,n}$  denotes the test statistic for the location that has the lesion for the n-th trial,  $\lambda_{0,n}$ , n denotes the test statistic for the locations without the lesion and  $u(\cdot)$  is the unit step function.

For SKEV task P is just a weighted sum of Equation (14) calculated for each type of signal weighted by the estimated prior probability of each signal. To calculate P for the SKS task, one must first calculate the sum-of-likelihood for a signal being present at each of the M locations as given in Equation (11). Using the sum-of-likelihood, P is estimated by

$$P = \frac{1}{N} \sum_{n=1}^N u(l_{1,n} - \max(l_{0,n})) \quad (15)$$

where  $N$  denotes the number of trials.

#### 4. Data Generation

The effects of varying the incident energy and the effect on the amount of fluence required to meet a preset image quality threshold (IQT) was examined. The IQT denotes the value of the image quality metric that the observer must perform equal to or better than in a given task. Energies ranging from 30 to 150 keV were tested. Data sets were generated at intervals of 5 keV for energies below 80 keV and intervals of 10 keV for 80 keV and above for a total of 18 distinct energy levels. For a user specified energy, the incident fluence was automatically varied across a range of 1,000 to 9,500,000 with 20 data points in each order of magnitude for a total of 80 data points. A vectorized image window of 24 x 24 pixels near the lesion were outputted as a data file for image quality analysis. Each dataset (at a specific energy and specific fluence) contained 50 vectorized image files with a lesion, 50 vectorized image files without a lesion, and the two corresponding raw image files of the entire chest for a grand total of 2,350,080 such images. Grid characteristics were held constant using 65 and 5 percent for the primary and scattered photon transmission rates respectively for all tasks. The detector quantum absorption efficiency (DQAE) was modeled after a cesium iodine screen as detailed in (Chan & Doi 1984). To take into account how absorption efficiency changes with energy, DQAE was changed depending on the energy of the incident photons and the average energy of the scattered photons. Table 1 shows the DQAE value for each energy level. Patient set up geometry was also held constant at 180 cm source-to-image distance with a 5 cm gap between the patient's back and the detector. For the SKE/BKE task, the simulated lesion was kept at a constant location in the left lung clear of ribs with a diamond shape. Attenuation of the lesion was kept constant at 400 HU. The HU value was chosen to represent a

calcified lesion (Erbel, Budde, Kerkhoff, Mohlenkamp & Schmermund 2002, Fayad & Fuster

Energy	30	35	40	45	50	55	60	65	70
DQAE	56	91	88	77	68	60	51	46	40

Energy	75	80	90	100	110	120	130	140	150
DQAE	34	31	23	18	14	10	7	5	4

**Table 1. DQAE in percentage for each energy level (in keV)**

	Locations	Tumor type	HU of tumor	Energy range
SKE/BKE	(1)	(a)	150, 400	30keV–150keV
2AFC	(1),(2)	(a)	400	30keV–150keV
3AFC	(1)-(3)	(a)	400	30keV–150keV
4AFC	(1)-(4)	(a)	400	30keV–150keV
SKEV	(1)-(4)	(a),(b)	400	30keV–150keV

**Table 2. Locations, tumor types, HU value, and energy level range used for each task type. Each location is denoted by a number: (1) left lung, (2) right lung with obstruction by a rib, (3) heart, (4) liver. Each tumor types (varied by the size) is denoted by a letter: (a) large (11 pixels), (b) small (7 pixels).**

2001). For the MAFC task, additional sets of data were generated at 3 additional lesion locations for maximum of  $M = 4$  locations. The locations were chosen so as to not overlap with each other to ensure the pairwise uncorrelated assumption. The lesion size and HU value was kept constant as in SKE/BKE task. Datasets with a smaller lesion were also generated for the SKEV task for total of 2 possible lesion sizes. The set of locations used for these tasks were the same as those used in the MAFC task. The lesions were roughly diamond shaped. The larger lesion used in all tasks was 11 pixels long along the diagonal. The smaller lesion generated for the SKEV task was 7 pixels long along the diagonal. Table 2 summarizes the locations, lesion types, and energy levels used for each task.

The vectorized images analyzed were 24 x 24 pixels centered on the simulated lesion location. Thirty images from each set of background and lesion images were randomly selected as the training set for the observers. Due to small sample size relative to the number of pixels (i.e. number

of dimensions), it was necessary to regularize the estimated covariance matrices in order to stabilize them. To this end, the regularized discriminant analysis method was employed as described in (Friedman 1989). Empirical regularization parameters were chosen through trial-and-error. In order to make all comparisons valid, regularization parameters were held fixed for all the experiments.

## 5. Optimization

Optimization of effective dose administered to the patient is performed in three steps. First, a series of image quality curves were constructed as a function of fluence for a fixed energy level. Next, the quality curves were examined for the lowest fluence level at which the image quality metric exceeds a chosen threshold. Thirdly, these fluence levels were converted to effective doses.

The first step in the process is task specific. As described previously, AUC is used as the image quality metric for SKE/BKE tasks requiring construction of series of ROC curves each at a fixed fluence and energy level. A sample ROC curve is shown in Figure 3. The quality curve for

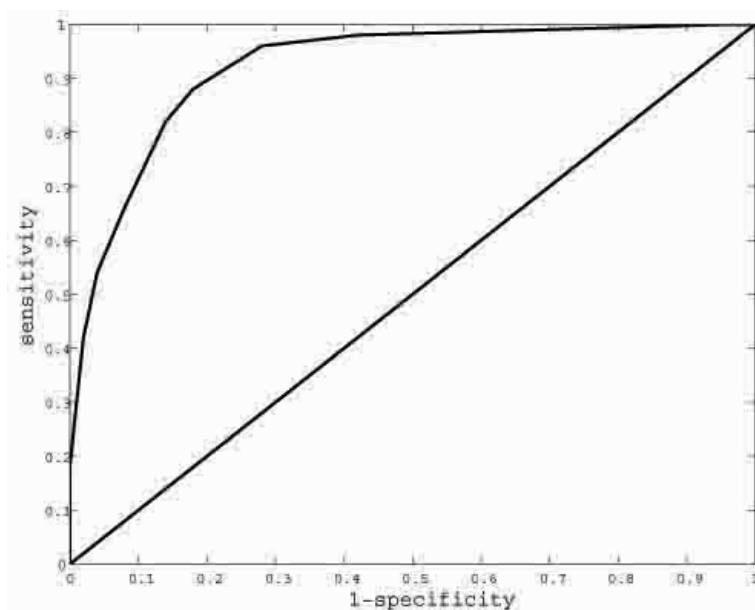


Figure 3. Plot of ROC curve for Laguerre-Gauss Hotelling observer at 70 keV and  $1,000,000 \text{ m}^{-2}$  fluence.

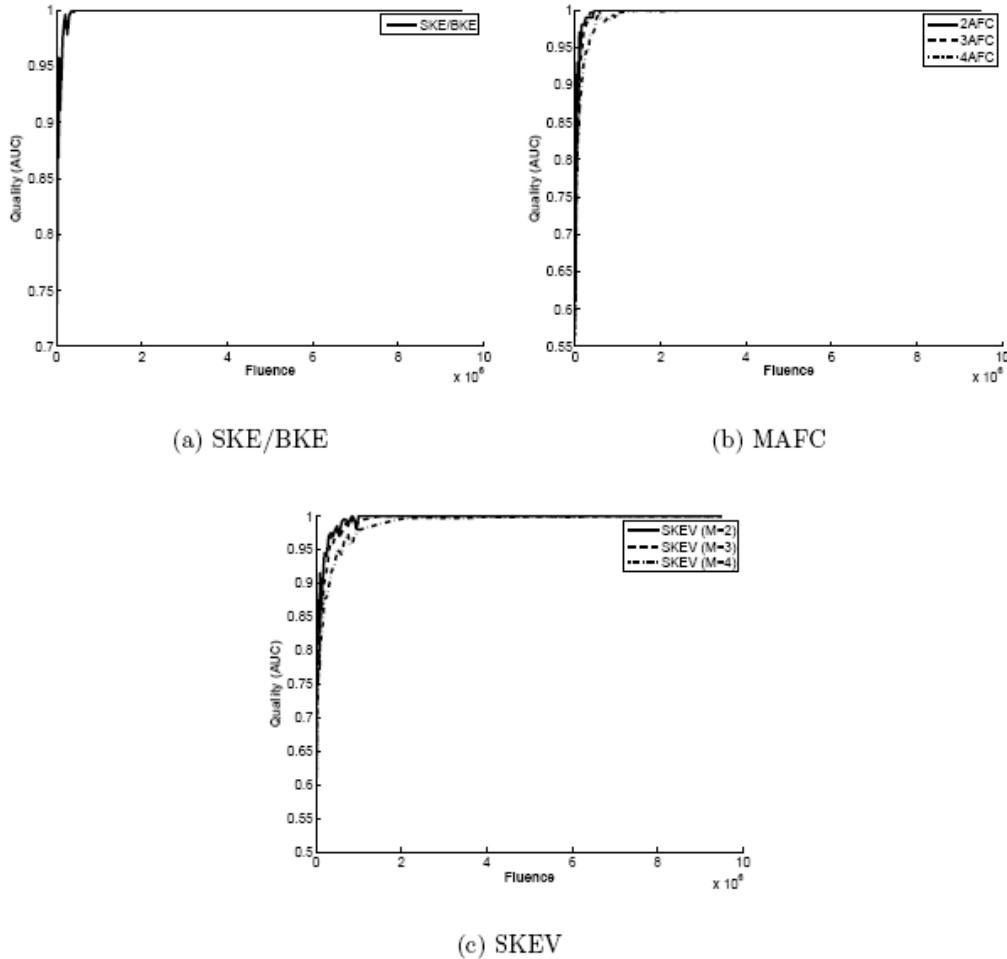
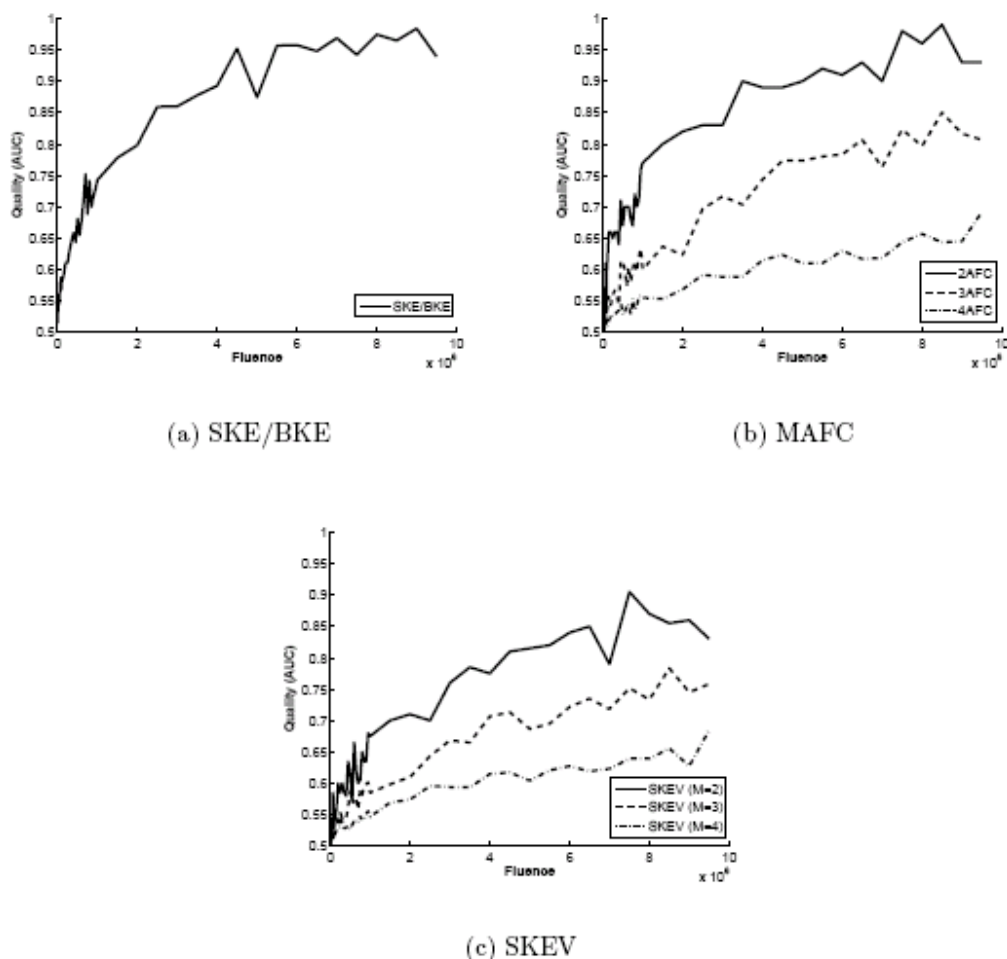


Figure 4. Plot of the quality measure vs. fluence for various tasks performed. The plot shown are fixed at 50keV. The plot shows the performance of Hotelling observer. The performance of the observer, i.e. the image quality metric, is, on average, decreased with addition of more location variations.

SKE/BKE task is then just the value of the AUC plotted against varying fluence for each energy. For MAFC, SKEV, and SKS tasks, their respective image quality metric, as described in Section 3.3, is used in lieu of AUC. Figures 4 and 5 show sample plots of these image quality curves for various tasks using Hotelling and Laguerre-Gauss Hotelling observers, respectively. Figure 4(a) shows the result for SKE/BKE task using Hotelling observer. The figure shows that the

performance is extremely good. Incorporating a more realistic observer model degrades the performance as expected (see Figure 5(a)). Addition of more location (MAFC) and lesion



**Figure 5. Plot of the quality measure vs. fluence for various tasks performed. The plot shown are fixed at 50keV. The plot shows the performance of Laguerre-Gauss Hotelling observer. The performance of the observer, i.e. the image quality metric, is, on average, decreased with addition of more location variations. Furthermore, compared with Figure 4, Laguerre-Gauss Hotelling performs worse than the Hotelling observer.**

variations (SKEV) also affects the performance as seen in Figures 4(b), 4(c), 5(b), and 5(c). Later, we will again compare the results of the two observers and the various tasks performed.

Once the image quality curves are generated, the next step is to examine these curves and identify the optimal fluence at each energy level. The optimality is defined as the lowest fluence at

which the image generated meets a predetermined minimum IQT. A single optimal fluence level is identified per energy level. Changing the IQT changes the optimal fluence level. In general, raising

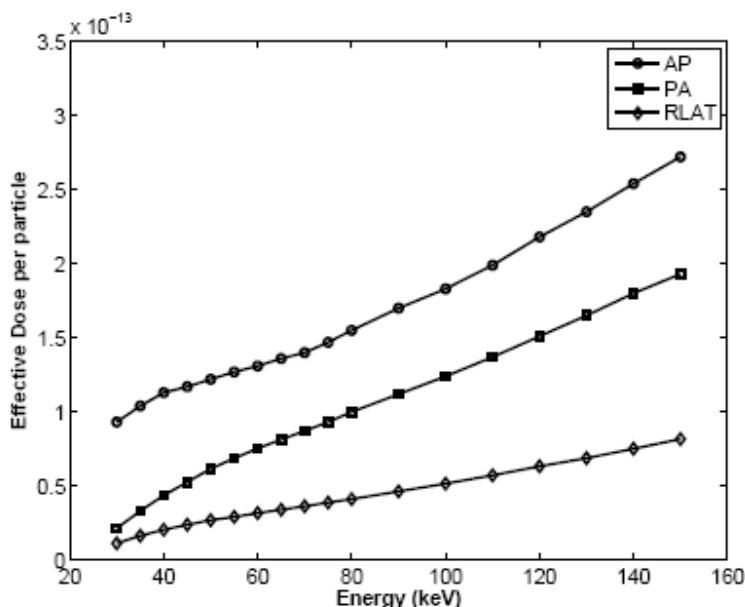


**Figure 6. Effective dose (mSv) per incident particle for various chest x-ray examination. (AP) - Anterior to Posterior, (PA) - Posterior to Anterior, (RLAT) - Right Lateral**

the IQT increases the optimal fluence.

The third step in the process is to convert the optimal fluence levels to their effective dose equivalent. The effective dose is a function of energy and the number of incident particles. The effective dose per incident particle for various chest x-ray configurations were previously calculated in (Winslow et al. 2004) for various monoenergetic fields. These calculations were then used to estimate the effective dosage per unit area using the optimal fluences. Figure 6 shows the effective dosage per particle calculated at each energy level as found in (Winslow et al. 2004). Using the effective dose calculations in (Winslow et al. 2004), the energy level and fluence at which the dose is minimized is then identified as optimal.

## 6. Results and Discussion

Figures 7–8 show the plots of optimal fluence vs. energy level for various tasks using Hotelling

and Laguerre-Gauss Hotelling observers, respectively. In order to save space and minimize redundant information, results for SKE/BKE, 3AFC, 4AFC, and SKEV (with M=3) are shown

IQT	Observer	Task	Effective Dose (mSv)	Energy (keV)	Fluence ( $m^{-2}$ )
0.6	HOT	SKE/BKE	1.13E-10	40	1000
		2AFC	1.17E-10	45	1000
		3AFC	2.925E-10	45	2500
		4AFC	4.27E-10	50	3500
		SKEV (M=2)	1.755E-10	50	2000
		SKEV (M=3)	3.51E-10	45	4000
		SKEV (M=4)	5.85E-10	45	5000
	CHOT	SKE/BKE	2.44E-8	50	200000
		2AFC	1.33E-8	50	100000
		3AFC	5.49E-8	50	450000
		4AFC	4.37E-7	60	3000000
		SKEV (M=2)	3.71E-8	45	350000
		SKEV (M=3)	1.16E-7	50	950000
		SKEV (M=4)	4.68E-7	45	4000000
0.7	HOT	SKE/BKE	1.13E-10	40	1000
		2AFC	4.68E-10	45	4000
		3AFC	1.08E-9	55	8500
		4AFC	1.97E-9	60	15000
		SKEV (M=2)	7.61E-10	45	5500
		SKEV (M=3)	2.04E-9	65	15000
		SKEV (M=4)	4.10E-9	45	35000
	CHOT	SKE/BKE	8.0E-8	45	700000
		2AFC	4.49E-8	45	450000
		3AFC	3.67E-7	50	3000000
		4AFC	N/A	N/A	N/A
		SKEV (M=2)	2.22E-7	50	2000000
		SKEV (M=3)	5.29E-7	55	4000000
		SKEV (M=4)	N/A	N/A	N/A
0.8	HOT	SKE/BKE	1.13E-10	40	1000
		2AFC	2.73E-9	45	20000
		3AFC	3.18E-9	55	25000
		4AFC	5.66E-9	45	55000
		SKEV (M=2)	3.18E-9	55	25000
		SKEV (M=3)	7.22E-9	45	60000
		SKEV (M=4)	1.05E-8	45	90000
	CHOT	SKE/BKE	8.0E-8	45	2500000
		2AFC	2.97E-7	55	2000000
		3AFC	3.67E-7	50	6500000
		4AFC	N/A	N/A	N/A
		SKEV (M=2)	5.27E-7	45	4500000
		SKEV (M=3)	N/A	N/A	N/A
		SKEV (M=4)	N/A	N/A	N/A
0.9	HOT	SKE/BKE	3.05E-9	50	25000
		2AFC	5.93E-9	55	55000
		3AFC	1.05E-8	45	90000
		4AFC	2.15E-8	45	200000
		SKEV (M=2)	1.10E-8	50	90000
		SKEV (M=3)	2.64E-8	50	200000
		SKEV (M=4)	4.07E-8	50	350000
	CHOT	SKE/BKE	5.27E-7	45	4500000
		2AFC	5.85E-7	45	5500000
		3AFC	N/A	N/A	N/A
		4AFC	N/A	N/A	N/A
		SKEV (M=2)	N/A	N/A	N/A
		SKEV (M=3)	N/A	N/A	N/A
		SKEV (M=4)	N/A	N/A	N/A

**Table 3. Fluence and the energy level at the optimal dose for various IQTs. The value, N/A, indicates that the optimal dose was off the range of fluence that were investigated. (HOT=Hotelling, CHOT=Laguerre-Gauss Hotelling)**

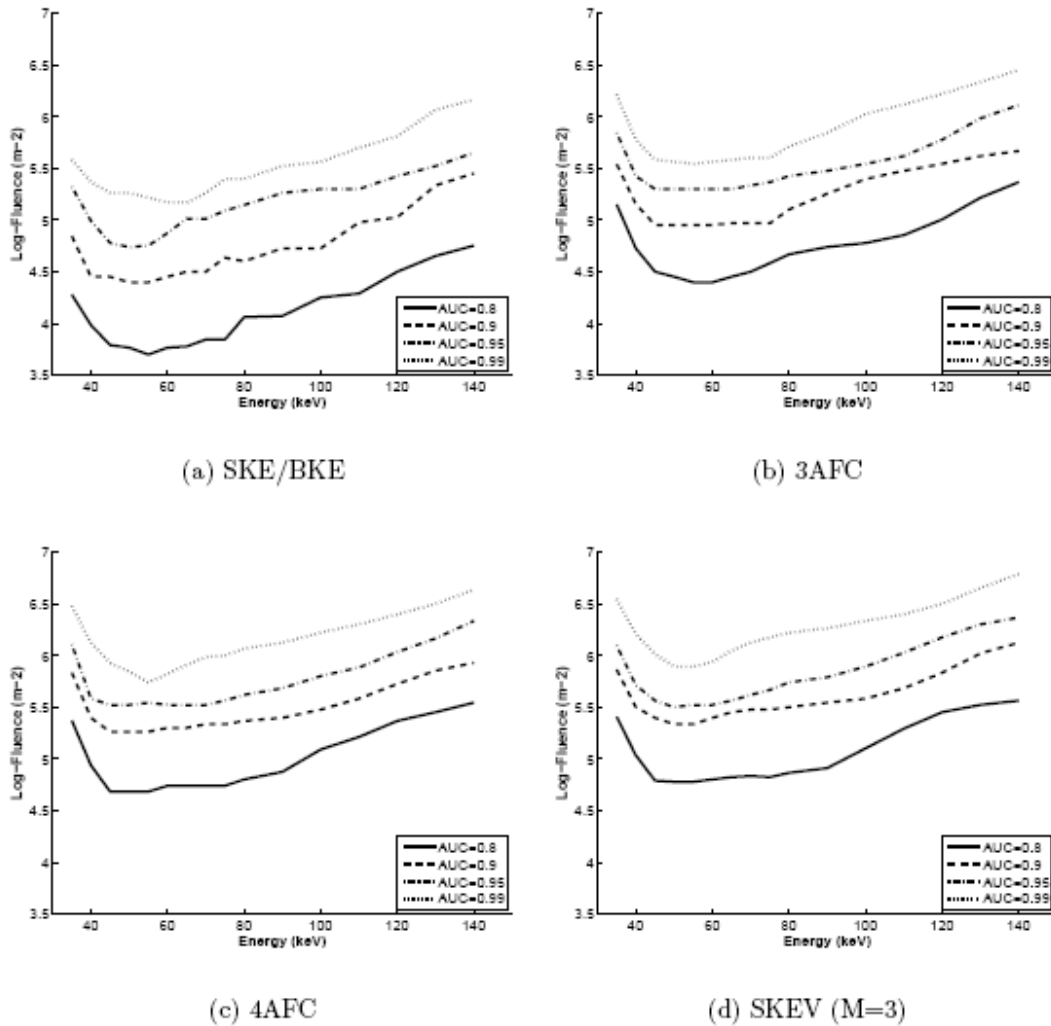


**Figure 7. The logarithm of the optimal fluence ( $m^{-2}$ ) vs. energy using Hotelling observer for (a) SKE/BKE, (b) 3AFC, and (c) SKEV (with  $M=3$ ) tasks. As the complexity of the task (i.e, number of location variations, number of lesion size variation) increases optimal fluence level also generally increases.**

only. The following discussion applies to all other remaining tasks not shown. The performance and optimal dosage are influenced by three difference variables, namely, number of locations, introduction of additional lesion type, and IQT variations. The effect of each on optimal dosage will be discussed in turn.

Looking at Figure 7, the graphs in Figure 7(b) are shifted up in fluence axis relative to graphs in

Figure 7(a). Similarly, graphs in Figure 7(c) are shifted up relative to Figures 7(b) and 7(a). The

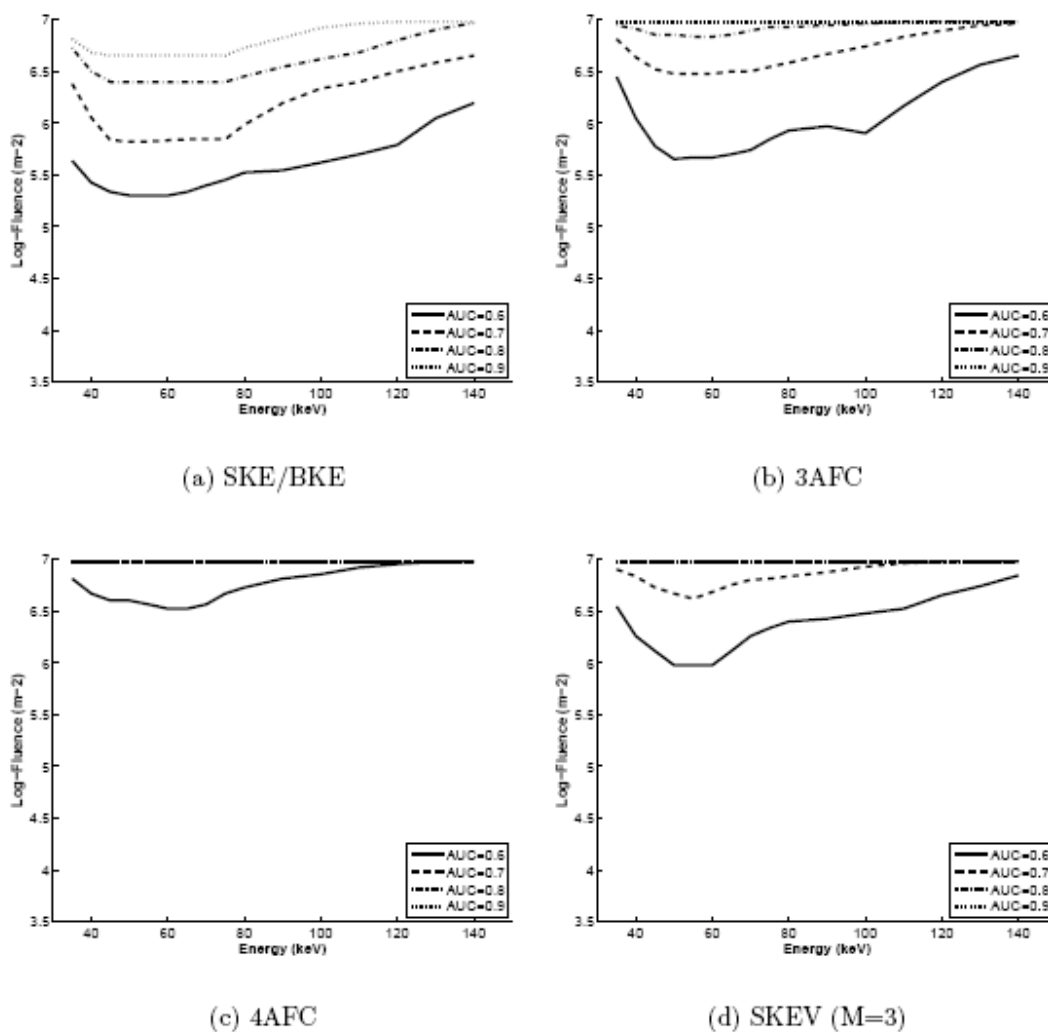


**Figure 8.** The logarithm of the optimal fluence ( $m^{-2}$ ) in log scale vs. energy using Laguerre-Gauss Hotelling observer for SKE/BKE, 2AFC, 3AFC, and SKEV (with  $M=3$ ) tasks.

graphs in Figure 8 exhibit a similar pattern. It is clear from this pattern that number of locations,  $M$ , affects the performance of the observer. This is not surprising, since increasing the number of locations increases the complexity of the task. More specifically, as the number of location variation increases lesion detectability decreases. This pattern is also evident in the image quality plots of the Laguerre-Gauss Hotelling observer shown in Figure 5. To a lesser extent, this is also evident from the image quality plots of Hotelling observer shown in Figure 4. It is more difficult to

differentiate between the performance of Hotelling observer for different values of  $M$  due to the

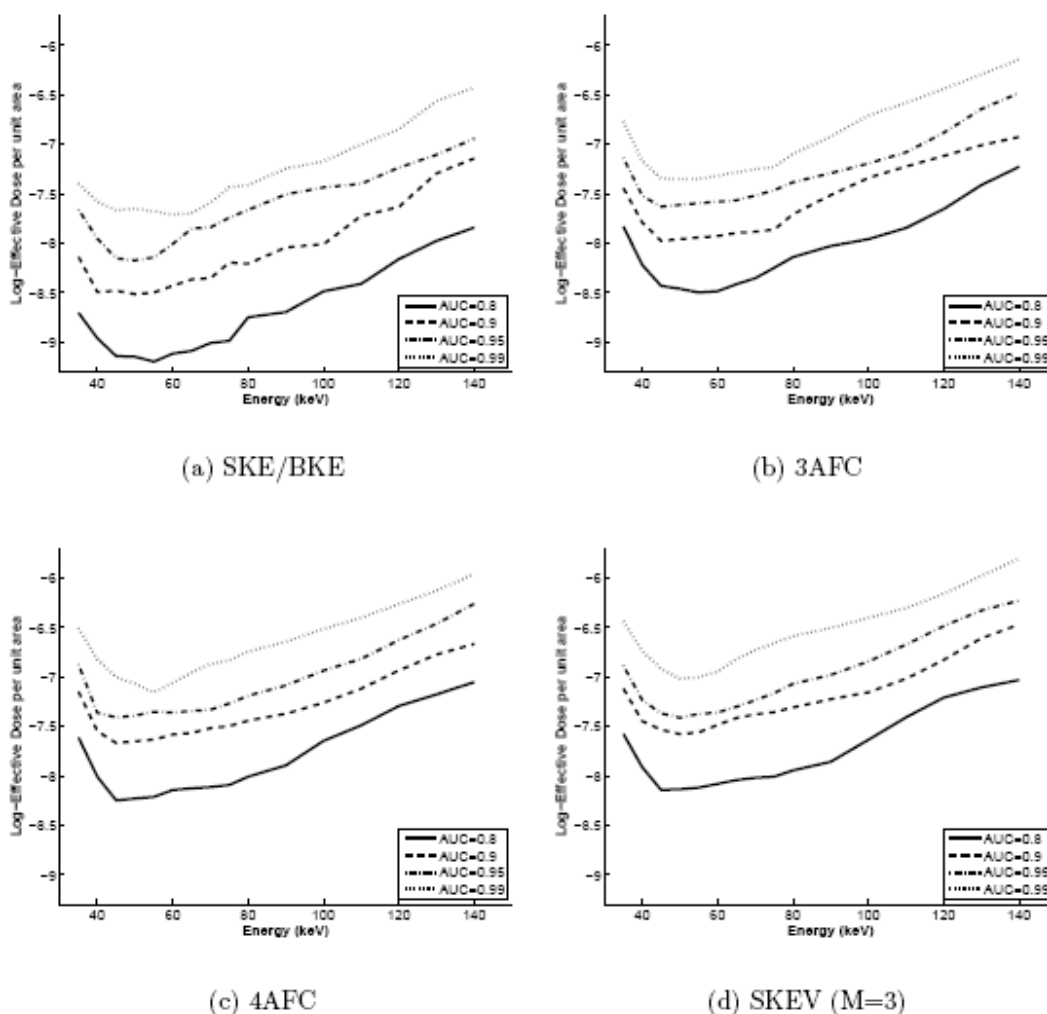


**Figure 9. Logarithm of effective dose (mSv) vs. energy level for SKE/BKE, 2AFC, 3AFC, and SKEV (with  $M=3$ ) tasks using Hotelling observer.**

fact that the observer performs well in all tasks. This is to be expected since the Hotelling observer is optimal among all linear observers under Gaussian assumption. It is also well established that the Hotelling observer outperforms human observers in all tasks (Eckstein & Abbey 2001). A more comparable performance to human is achieved using Laguerre-Gauss Hotelling observer. The effect of increased fluence requirement for increasing  $M$  generally increases the dosage required. This can be assessed from comparing figures 9(a), 9(b), and 9(c) for Hotelling observer

and 10(a), 10(b), and 10(c) for Laguerre-Gauss Hotelling observer which exhibits an analogous

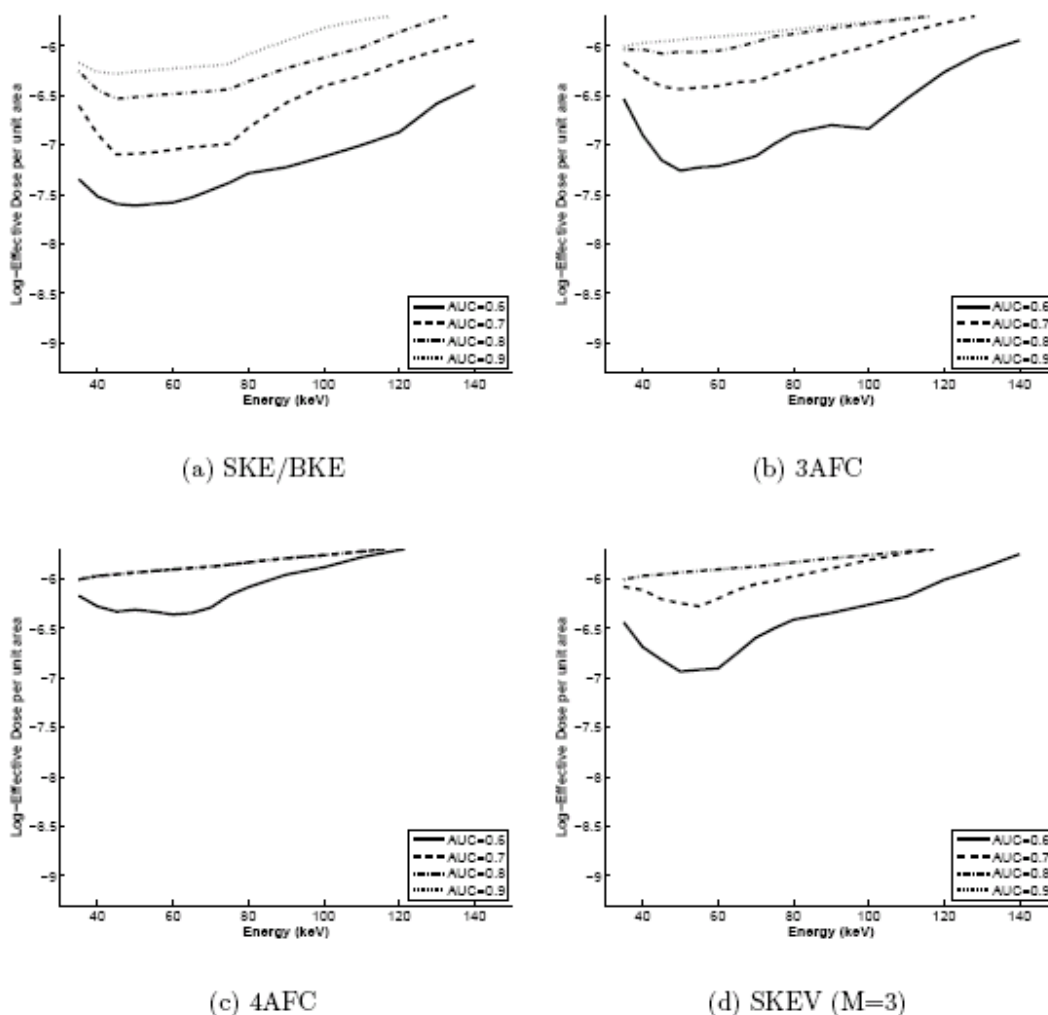


**Figure 10. Logarithm of effective dose (mSv) vs. energy level for SKE/BKE, 2AFC, 3AFC, and SKEV (with M=3) tasks using Laguerre-Gauss Hotelling observer.**

shift upwards in dosage. These results conform with the results from previous experiments with MAFC task such as (Burgess & Ghandeharian 1984, Burgess 1994, Eckstein & Whiting 1996, Kijewski, Mueller & Moore 1992, Bochud, Abbey & Eckstein 2003). In all of these studies, it was found that the number of lesion locations degraded the performance of the model (and/or human) observers as observed in the present study. The degradation of the observer performance in turn increases the dosage requirement for target IQT.

Increasing the IQT also affects the value of the optimal fluence. In all of the results for both Hotelling (Figure 7) and Laguerre-Gauss Hotelling (Figure 8) observers, increasing the target IQT shifts the graph upwards in fluence axis. The reason is simply because it becomes more difficult for the model observer to achieve the desired level of performance as indicated by the IQT, i.e. the observer must detect more lesions correctly. The increased IQT hence increases the optimal fluence. The corresponding energy level at which the lowest optimal fluence is achieved, however, does not vary consistently with increased IQT (or with increased  $M$ ). The results indicate that the energy level at which the lowest fluence is achieved ranges from 45 to 65 keV. The fluctuation in energy level corresponding to the optimal fluence may be due to the small number of energy samples (18 in all). Figures 9–10 show the conversion of the optimal fluences to their respective effective doses. Table 3 tabulates the lowest dosage in these graphs with their corresponding energy levels for several IQT values. The optimal dose is usually achieved at the energy level corresponding to the lowest fluence and spans the range of 45 to 65 keV. It is important to keep in mind, however, that there is a relatively positive relationship between the energy and the effective dose calculations as shown in Figure 6. The effect of this positive slope can be seen in some instances. For example, examining the graphs in Figure 7(b) shows that the lowest fluence is achieved at around 55–60 keV for IQT value of 0.8. However, the lowest effective dose is actually achieved at 45 keV as shown in Table 3.

The addition of lesion size variation further degrades the performance of the observers as task complexity is increased. This can be seen from the results in Figures 7–10, and in Table 3. These results show that the optimal fluence and effective dose for SKEV task rises relative to MAFC task with equal value of  $M$ . For example, comparing Figure 7(b) with Figure 7(d), the fluence values are generally larger per energy level for SKEV task than for

MAFC of equal M value. The performance degrading effect of introducing lesion size variation agrees with previous studies such as (Eckstein & Abbey 2001, Eckstein, Zhang, Pham & Abbey 2003).

To summarize, although the optimal effective dose has a clear positive correlation with the complexity of the task, the energy level at which the optimal effective dose value is achieved shows no such relationship in our simulations. Neither the increase in the number of background variations nor the lesion variations have predictable effect on the energy level at which the optimal effective dose is achieved. As discussed above, this may be due to the limited number of energies and task complexities we examined.

## **7. Conclusions and Future Works**

The goal of this study is to show the feasibility of determining the optimal dose administered to a patient using a chain of computer simulations. Towards this goal, we have developed an image quality analysis software in MATLAB and coupled it with an x-ray imaging simulator, ViPRIS. We have demonstrated that an x-ray simulator with computerized observers can be utilized in radiography dose optimization. It is found that, for the subject and the methods we employed, the optimal x-ray energy ranges from 45 to 65 keV. Further research will examine the clinical implication of these methods.

The key focus of the study was to digitize the entire optimization process, where every component was modeled in a computer simulation. This has the advantage of reducing human labor and being cost effective and time efficient. Previous studies have demonstrated that computerized observer models such as channelized Hotelling and NPWE perform comparable to human observers. Modifications to the basic SKE/BKE observer task in the form of location and lesion variations also provide more clinically realistic scenarios.

There are a number of limitations currently present with our simulation system. Our system employs single phantom capable of simulating a chest x-ray only. A more advanced phantom and/or phantoms of several different individuals with different bodytypes may be desirable. The computerized observer package may be expanded to include observer models with more accurate representation of the human eye, such as channelized Hotelling model with Gabor filters as described in (Zhang, Pham & Eckskein 2004) and non-pre whitening eye filter as described in (Eckstein et al. 2000). In addition, it has been noted previously, that even under noise free conditions, human observer response varies (Burgess, Humphrey & Wagner 1979, Burgess 1981, Burgess & Colborne 1988). This variation is attributed to the general notion of “internal noise”. The internal noise may be modeled by further randomizing the observer’s response around the chosen threshold point as suggested in (Ahumada, Jr. 2002). Future generations of the system will incorporate improvements to these areas and provide a more rigorous data processing and image generation algorithms comparable to proprietary software used in contemporary imaging systems.

### **Acknowledgments**

We wish to thank Dr. Walter Huda, Dr. Kent Ogden and Dr. Ernest Scalzetti of the Department of Radiology, State University of New York, Upstate Medical University for their guidance and input on the clinical realism of the simulator. Various portions of this research were supported by the Center for Subsurface Sensing and Imaging Systems, under the Engineering Research Center Program of the National Science Foundation Award Number EEC-9986821), and Rensselaer Polytechnic Institute. In addition, research associated with computational VIP-Man model was supported during this project by grants to Dr. X. G. Xu from National Science Foundation (BES-9875532) and National Institutes of Health (1 R03 LM007964-01). Any opinions, findings, and conclusions or recommendations expressed in this material are those of the authors and do not

necessarily reflect the views of the National Science Foundation or the National Institutes of Health.

## References

- Abbey, C. K., Barrett, H. H. & Eckstein, M. P. (1997). Practical issues and methodology in assessment of image quality using model observers, *Proceedings of SPIE*, Vol. 3032, SPIE, pp. 182–194.
- Agarwal, S., Graepel, T., Herbrich, R., Har-Peled, S. & Roth, D. (2005). Generalized bounds for area under the roc curve, *Journal of Machine Learning Research* 6: 393–425.
- Ahumada, Jr., A. J. (2002). Classification image weights and internal noise level estimation, *Journal of Vision* 2: 121–131.
- Barrett, H. H., Abbey, C. K., Gallas, B. & Eckstein, M. P. (1998). Stabilized estimates of Hotelling- observer detection performance in patient-structured noise, *Proc. SPIE Vol. 3340*, p. 27-43,
- Medical Imaging 1998: Image Perception*, Harold L. Kundel; Ed., pp. 27–43.
- Bochud, F. O., Abbey, C. K. & Eckstein, M. P. (2003). Search for lesions in mammograms: statistical characterization of observer responses, *Medical Physics* 31(1): 24–36.
- Box, G. E. P. & Muller, M. E. (1958). A note on the generation of random normal deviates, *Annals of Mathematical Statistics* 29: 610–611.
- Burgess, A. (1994). Statistically defined backgrounds: performance of a modified nonprewhitening observer model, *J. Opt. Soc. Am. A* 11(4): 1237–1242.
- Burgess, A. E. (1981). Density dependence of signal detection in radiographs, *Medical Physics* 8(5): 646–651.
- Burgess, A. E. & Colborne, B. (1988). Visual signal detection. iv. observer inconsistency, *Journal*

of Optical Society of America 5(4): 617–627.

Burgess, A. E. & Ghandeharian, H. (1984). Visual signal detection. ii. signal-location identification, *Journal of Optical Society of America* 1(8): 906–910.

Burgess, A. E., Humphrey, K. & Wagner, R. F. (1979). Detection of bars and discs in quantum noise, in J. Gray (ed.), *Proc. Soc. Photo-Opt. Instrum. Eng.: Application of Optical Instrumentation in Medicine VII*, Vol. 173, pp. 34–40.

Chan, H.-P. & Doi, K. (1984). Studies of x-ray energy absorption and quantum noise properties of x-ray screens by monte carlo simulation, *Med. Phys.* 11(1): 37–46.

Eckstein, M. P. & Abbey, C. K. (2001). Model observers for signal known statistically task, in D. P.

Chakraborty & E. A. Krupinski (eds), *Proceedings of SPIE*, Vol. 4324, SPIE, pp. 91–102.

Eckstein, M. P., Abbey, C. K. & Bochud, F. O. (2000). A practical guide to model observers for visual detection in synthetic and natural noisy images, *Handbook of Medical Imaging Vol. I: Physics and Psychophysics*, SPIE Press, pp. 593–628.

Eckstein, M. P., Bartroff, J. L., Abbey, C. K., Whiting, J. S. & Bochud, F. O. (2003). Automated computer evaluation and optimization of image compression of x-ray coronary angiograms for signal known exactly detection tasks, *Optics Express* 11(5): 460–475.

Eckstein, M. P. & Whiting, J. S. (1996). Visual signal detection in structured backgrounds i. effect of number of possible spatial locations and signal contrast, *Journal of Optical Society of America* 13(9): 1777–1787.

Eckstein, M. P., Zhang, Y., Pham, B. & Abbey, C. K. (2003). Optimization of model observer performance for signal known exactly but variable tasks leads to optimized performance in signal known statistically tasks, in D. P. Chakraborty & E. A. Krupinski (eds), *Proc. SPIE Vol.5034*,

Medical Imaging 2003: Image Perception, Observer Performance, and Technology Assessment, pp. 123–134.

Erbel, R., Budde, T., Kerkhoff, G., Mohlenkamp, S. & Schmermund, A. (2002). Understanding the pathophysiology of the arterial wall: which method should we choose? electron beam computed tomography, *European Heart Journal Supplements* 4: F47–F53.

Fayad, Z. A. & Fuster, V. (2001). Clinical imaging of the high-risk or vulnerable atherosclerotic plaque, *Circulation Research* 89: 305–316.

Friedman, J. (1989). Regularized discriminant analysis, *Journal of American Statistical Association* 84: 165–175.

ICPR (1975). International Commission on Radiological Protection: Report of Task Group on Reference Manual (ICRP 23), Pergamon Press, Oxford.

ICPR (1991). International commission on radiological protection, publication 60: 1990 recommendations of the icpr, *Annals of the ICPR* 21(1–3).

Kawrakow, I. & Rogers, D. W. O. (2003). The egsnrc code system: Monte carlo simulation of electron and photon transport, National Research Council of Canada pp. 1–289.

Kijewski, M. F., Mueller, S. P. & Moore, S. C. (1992). The barankin bound: a model of detection with location uncertainty, in D. C. Wilson & J. N. Wilson (eds), *Proc. SPIE Vol. 1768, Mathematical Methods in Medical Imaging*, David C. Wilson; Joseph N. Wilson; Eds., pp. 153–160.

Lazos, D., Bliznakova, K., Kolitsi, Z. & Pallikarakis, N. (2003). An integrated research tool for x-ray imaging simulation, *Computer Methods and Programs in Biomedicine* 70(3): 241–251.

Myers, K. J. & Barrett, H. H. (1987). Addition of a channel mechanism to the ideal-observer

model,

*Journal of Optical Society of America* 4(12): 2447–2457.

Pineda, A. R. & Barret, H. H. (2004a). Figures of merit for detectors in digital radiography. i. flat background and deterministic blurring, *Med. Phys.* 31(2): 348–358.

Pineda, A. R. & Barret, H. H. (2004b). Figures of merit for detectors in digital radiography. ii.

Finite number of secondaries and structured backgrounds, *Med. Phys.* 31(2): 359–367.

Sandborg, M., McVery, G., Dance, D. R. & Carlsson, G. A. (2001). Schemes for the optimization of chest radiography using a computer model of the patient and x-ray imaging system, *Medical Physics* 28: 2007–2019.

Spitzer, V. M. & Whitlock, D. G. (1998). *Atlas of the Visible Human Male*, Jones and Bartlett Publishers.

Suryanarayanan, S., Karellas, A., Vedantham, S., Ved, H. & D’Orsi, C. J. (2003). Evaluation of detection in compressed digital mammograms using numerical observers, in D. P. Chakraborty & E. A. Krupinski (eds), *Proceedings of SPIE*, Vol. 5034, SPIE, pp. 513–521.

UN (2000). *Sources and effects on ionizing radiation.*, Technical report, United Nations Scientific Committee on the Effects of Atomic Radiation (UNSCEAR), New York.

Winslow, M., Huda, W., Xu, X. G., Chao, T. C., Shi, C. Y., Ogden, K. M. & Scalzetti, E. M. (2004). Use of the vip-man model to calculate energy imparted and effective dose for x-ray examinations, *Health Physics* 86(2): 174–182.

Winslow, M. P. (2005). *Simulation of radiographic images for quality and dose analysis.*, Phd. dissertation, Rensselaer Polytechnic Institute, Troy, NY.

Winslow, M., Xu, X. G. & Yazici, B. (2005). Development of a simulator for radiographic image optimization, *Computer Methods and Programs in Biomedicine* 78(3): 179–190.

- Xu, X. G., Chao, T. C. & Bozkurt, A. (2000). Vip-man: An image-based whole-body adult male model constructed from color photographs of the visible human project for multi-particle monte carlo calculations, *Health Physics* 78(5): 476–486.
- Yao, J. & Barrett, H. H. (1992). Predicting human performance by a channelized Hotelling observer model, *Proc. SPIE Vol. 1768*, p. 161-168, *Mathematical Methods in Medical Imaging*, David C. Wilson; Joseph N. Wilson; Eds., pp. 161–168.
- Yendiki, A. & Fessler, J. A. (2005). Analysis of observer performance in known-location tasks for tomographic image reconstruction, *IEEE Transactions on Medical Imaging* .
- Zhang, Y., Pham, B. T. & Ecsktein, M. P. (2004). Automated optimization of jpeg 2000 encoder options based on model observer performance for detecting variable signals in x-ray coronary angiograms, *IEEE Transactions on Medical Imaging* 23(4): 459–474.
- Zhao, B., Schwarz, L. H. & Kijewski, P. K. (1998). Effects of lossy compression on lesion detection: Predictions of the nonprewhitening matched filter, *Med. Phys.* 25(9): 1621–1624.